Realizing quantum optics in structured environments with giant atoms

Xin Wang [1], Huai-Bing Zhu,[1] Tao Liu,[2] and Franco Nori [3,4,5]

[1]*Institute of Theoretical Physics, School of Physics, Xi'an Jiaotong University, Xi'an 710049, People's Republic of China*
[2]*School of Physics and Optoelectronics, South China University of Technology, Guangzhou 510640, China*
[3]*Center for Quantum Computing, RIKEN, Wakoshi, Saitama 351-0198, Japan*
[4]*Theoretical Quantum Physics Laboratory, Cluster for Pioneering Research, RIKEN, Wakoshi, Saitama 351-0198, Japan*
[5]*Physics Department, University of Michigan, Ann Arbor, Michigan 48109-1040, USA*

To go beyond quantum optics in free-space setups, atom-light interfaces with structured photonic environments are often employed to realize unconventional quantum electrodynamics (QED) phenomena. However, when employed as quantum buses, those long-distance nanostructures are limited by fabrication disorders. In this work, we alternatively propose to realize structured light-matter interactions by engineering multiple coupling points of hybrid giant atom–conventional environments without any periodic structure. We present a general optimization method to obtain the real-space coupling sequence for multiple coupling points. We report a broadband chiral emission for frequency-tunable giant emitters, with no analog in other quantum setups. Moreover, we show that the QED phenomena in the band-gap environment, such as fractional atomic decay and dipole-dipole interactions mediated by a bound state, can be observed in our setup. Numerical results indicate that our proposal is robust against fabrication disorders of the coupling sequence. Our work opens up a route for realizing unconventional light-matter interactions.

I. INTRODUCTION

Harnessing interactions between quantum emitters and quantized electromagnetic fields is a central topic of quantum optics [1–6]. In recent years, a burgeoning paradigm with giant atoms, which are coupled to waveguides at multiple separate points with their sizes comparable to photonic wavelengths, provides unanticipated opportunities to gain insights into exotic quantum optics beyond the dipole approximation [7–21]. The nonlocal coupling points cause nontrivial phase accumulation of the propagating field from a single giant emitter [22–24], allowing us to observe exotic phenomena with no analog in small-atom setups. The examples include decoherence-free interaction and oscillating bound states, which are caused by quantum interference and time-delay effects, respectively [25–27].

Structured dielectric environments, which are scalable in integrated chips, have achieved tremendous progresses in quantum optics [28–34]. Compared with free-space setups, the vacuum mode properties and dispersion relation can be tailored freely by shaping the dielectric structures [35–41]. One emblematic example is photonic crystal waveguides (PCWs), where the dielectric profile is periodically modulated, leading to the appearance of band gaps [42–48]. Inside the gap, stable bound states of the hybrid photon and emitter are formed, which can alternatively mediate long-range interactions between emitters [49–57]. Moreover, when light is

tightly transversely confined in high-refractive-index materials, chiral emission occurs in nanophotonic structures owing to spin-momentum locking [58–65]. However, fabricating long-distance nanostructures is very challenging when configuring those nanophotonic materials as quantum buses for quantum information processing [51,52]. Due to unavoidable fabrication disorders and defects, photons are scattered repeatedly, and their fragile quantum coherence is destroyed [66–69].

Here we show that structured light-matter interactions can be realized from the viewpoint of giant atoms, i.e., by spatially designing the coupling sequence with a conventional photonic waveguide without any periodic structure. We present a general optimization method to obtain real-space coupling sequences for a target structured environment, which has never been discussed in previous studies. As examples, we show that both broadband chiral emission for frequency-tunable giant emitters (with no analog in other quantum setups) and band-gap effect scan be realized by considering tens of coupling points in a conventional one-dimensional (1D) waveguide. Numerical results indicate that our proposal is robust against fabrication disorders in the coupling sequences, and can avoid localization and decoherence of photons appearing in long-distance nanostructures.

II. OPTIMIZING THE COUPLING SEQUENCE

The generic Hamiltonian of a quantum emitter interacting with a bosonic bath can be written as (setting $\hbar = 1$)

$$H_{\text{int}} = \sum_k \Delta_k a_k^\dagger a_k + \sum_k G_k(a_k^\dagger \sigma_- + \text{H.c.}), \qquad (1)$$
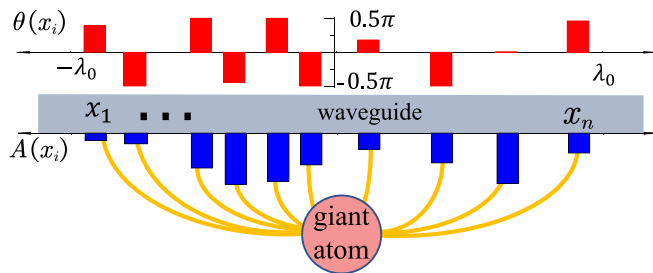
FIG. 1. Sketch of our proposal: A giant atom couples to a conventional 1D waveguide at positions $x_1, \ldots, x_N$. The coupling sequence $g(x_i) = A(x_i)e^{i\theta(x_i)}$ is obtained via optimization methods.

where $\Delta_k = \omega_k - \omega_q$, with ω_q being the giant atomic transition frequency. Assuming a giant atom interacting with the waveguide at multiple points $X = \{x_1, \ldots, x_N\}$ (see Fig. 1), the k-space interaction is thus written as

$$G_k = \sum_{x_i} g(x_i)e^{-ikx_i}, \quad g(x_i) = A(x_i)e^{i\theta(x_i)},$$

where $g(x_i)$ is the interaction strength at x_i (see Fig. 1). For small-atom setups, G_k is approximately a constant due to the pointlike coupling between the emitter and waveguide. Therefore, the structural engineering of the photonic waveguide's dispersion relation Δ_k plays an important role in achieving exotic quantum dynamics in previous studies [70–74]. In contrast, for our proposal, the bosonic environment is no longer designed, and a conventional waveguide is used. It has a linearized dispersion within the photonic bandwidth to which the giant atom significantly couples, i.e., $\omega_k = c|k|$ with c being the group velocity. An intuitive method for realizing the desired G_k is to find the real-space function $g(x_i)$ via inverse Fourier transformation (iFT) [8]. However, our following discussions indicate that this method has many problems and introduces many experimental overheads.

A. Analytical method and its problems

We assume giant atoms interacting with a 1D waveguide, which has a linearized dispersion within the photonic bandwidth to which the giant atom significantly couples. The following k-space coupling function equivalently describes an atom interacting with a band-gap environment,

$$G_k^I = \begin{cases} 0, & \left\{k_0 - \frac{k_d}{2} < |k| < k_0 + \frac{k_d}{2}\right\}, \\ G_0, & \left\{k_0 + \frac{k_d}{2} < |k| < k_{max}\right\}, \\ G_0, & \left\{-k_0 + \frac{k_d}{2} < k < k_0 - \frac{k_d}{2}\right\}. \end{cases} \quad (2)$$

That is, the gap's width is k_d and is centered at $\pm k_0$. The coupling constant is denoted by G_0. For convenience the ultraviolet cutoff frequency is set at ck_{max}, which should be large enough to approximate the regime $\{k_0 + \frac{k_d}{2} < |k| < k_{max}\}$ as an infinite-bandwidth environment.

The inverse Fourier transform (iFT) of G_k^I is derived as

$$g_I(x) = \frac{\sin k_{max}x}{\pi x} - 2\frac{\sin k_d x/2}{\pi x}\cos k_0 x, \quad (3)$$

which is a continuous function in real space. In experiments, giant atoms usually couple at multiple discretized positions on a waveguide. Therefore, we assume that the coupling function

$g_I(x)$ is sampled by the following function,

$$S(x) = W(x)P(x), \quad W(x) = \begin{cases} 1, & |x| \leqslant L, \\ 0, & |x| > L, \end{cases}$$

$$P(x) = \sum_{n=-\infty}^{n=+\infty} \delta(x - nX_T), \quad (4)$$

where $W(x)$ is a window function with a width $2L$, and $P(x)$ is the sample sequence composed by δ-function series which are equally spaced with distance X_T. To avoid retardation effects, the total coupling length $2L$ (i.e., the giant atom's size) should be much smaller than the size of the decaying photonic wave packet [26]. All those physical constraints will be addressed below.

According to the convolution theorem, the Fourier transformation of $S(x)$ is written as

$$S(k) = W(k) * \Delta(k), \quad W(k) = 2\frac{\sin(kL)}{k},$$

$$P(k) = \frac{2\pi}{X_T} \sum_{n=-\infty}^{n=\infty} \delta\left(k - \frac{2\pi n}{X_T}\right), \quad (5)$$

where $*$ represents the convolution of two functions. Equation (5) indicates that the width of the δ functions $\delta(k - \frac{2\pi n}{X_T})$ in k space are broadened as $\sim 2\pi/L$. To resolve the narrow band gap, the following relation should be satisfied,

$$2\pi/L \ll k_d \longrightarrow L \gg \frac{2\pi}{k_d}. \quad (6)$$

Additionally, to avoid the spectrum aliasing effect, the sample distance is bounded by the Nyquist-Shannon sampling theorem

$$\frac{2\pi}{X_T} \gg 2k_{max} \longrightarrow X_T \ll \frac{\pi}{k_{max}}. \quad (7)$$

Consequently, the coupling number of the giant atom is bounded by

$$N = \frac{2L}{X_T} \gg \frac{4k_{max}}{k_d}. \quad (8)$$

We now consider the target k-space coupling function with $k_{max} = 2k_0$ and $k_d = 1/15$ [see Fig. 2(a)]. According to Eq. (8), the minimum coupling number is calculated as $N = 120$. In Fig. 2(d), we plot the sampled real-space coupling sequence by setting $N = 300$. The corresponding k-space coupling function is shown in Fig. 2(a), and the amplitude is mapped with color in Fig. 2(b). Note that $\lambda_0 = 2\pi/k_0$ is the wavelength of the central mode in the gap, and is employed as the unit length in this work. The unit for the frequency is adopted as $\omega_c = ck_0$. To mimic the band gap, the most important feature of G_k is the vanishing of the coupling strength around k_0. The enlarged plot of this regime is depicted in Fig. 2(c), which shows that the remnant coupling is still about $0.02G_0$. In principle one can keep increasing both N and L to suppress the nonzero coupling. However, many more coupling points are needed, which is very challenging in experiments. Moreover, given that L is comparable to the wave packet decaying from a single point, the propagating time cannot be neglected.

Additionally, we note that the coupling strengths $g(x_i)$ which are sampled from Eq. (3) alter their signs [see
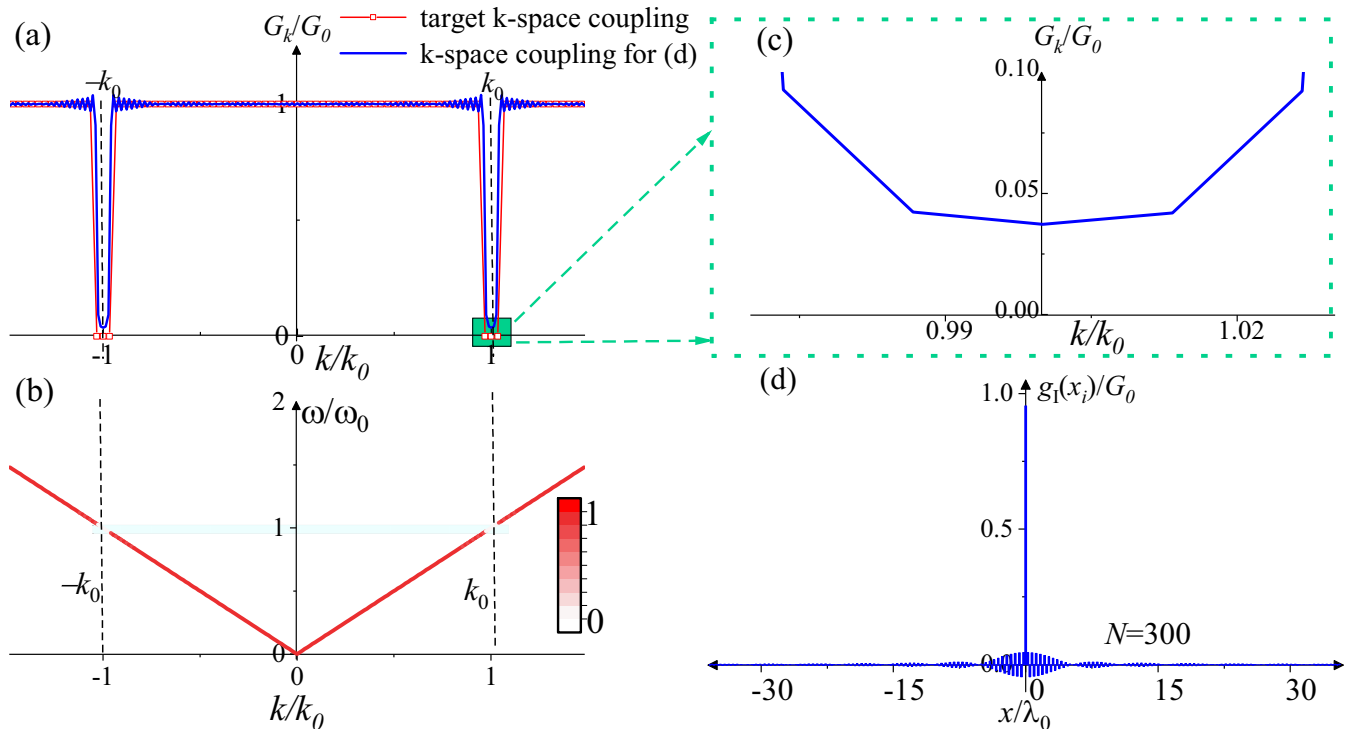
FIG. 2. (a) The k-space coupling for the real-space sequence by discretizing $g_I(x)$ in Eq. (3) [see plot in (d)]. The target coupling function has two symmetric dips centered at k_0 with width $k_d/k_0 = 1/15$. (b) The waveguide is assumed to be of linear dispersion with a phase velocity c. The coupling strength G_k in (a) is mapped with color, where two symmetric dips around k_0 are equivalent to band gaps in a structured environment. (c) The enlarged plot around k_0 of plot (a). Inside the band gap there is still remnant nonzero coupling ($\sim 0.02 G_0$) even with a large sampling number $N = 300$. (d) Real-space coupling sequence $g(x_i)$ (with $N = 300$). The sampling interval and total length are set as $X_T = 0.24\lambda_0$ and $L = 35\lambda_0$, respectively.

Fig. 2(d)]. That is, $g(x_i)$ needs an additional π-phase difference, which leads to another problem when implementing the coupling sequence in experiments. We now consider the circuit QED as an example, where giant atoms are mostly discussed. As depicted in Fig. 3, a transmon (working as a giant atom) is capacitively coupled to a 1D waveguide at multiple points. As discussed in Refs. [5,75], the interaction strength is written as

$$G_k = \sum_{x_i} g(x_i) e^{-ikx_i}, \qquad (9)$$

$$g(x_i) = \frac{e}{\hbar} \frac{C_g(x_i)}{C_\Sigma} \sqrt{\frac{\hbar \omega_k}{C_t}} \simeq \frac{e}{\hbar} \frac{C_g(x_i)}{C_\Sigma} \sqrt{\frac{\hbar \omega_q}{C_t}}, \qquad (10)$$
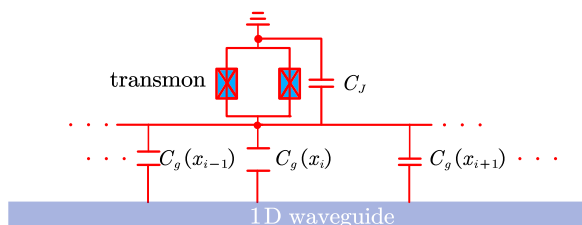

FIG. 3. Sketch of a feasible setup to realize our proposal: a transmon couples to a 1D coplanar waveguide at multiple coupling points via local capacitances $C_g(x_i)$. The real-space discretized coupling function is encoded into the capacitance sequence $C_g(x_i)$.

where C_J is the Josephson capacitance of the transmon, $C_g(x_i)$ is the coupling capacitance at point x_i, $C_\Sigma = C_J + \sum_i C_g(x_i)$, and C_t is the total capacitance of the waveguide. In Eq. (10) we replace $\omega_k \to \omega_q$ for the zero-point fluctuations of the voltage operators because only modes around ω_q contribute significantly to the dynamics. Under this condition, the local coupling strength $g(x_i)$ is proportional to the coupling capacitance $C_g(x_i)$, and the coupling sequence in Fig. 2(d) can be directly encoded into $C_g(x_i)$ (see Fig. 3). We notice that the coupling signs of $g(x_i)$ are fixed because $\{C_g(x_i), C_\Sigma\} \geqslant 0$. That is, there are no additional π-phase differences between different coupling points, and the discretized coupling obtained via the iFT method cannot be implemented with a linear coupling capacitance (or inductance). The additional local phase $\theta(x_i)$ can be encoded at x_i via the time-dependent modulating of the nonlinear QED elements, which however will add more overheads in the experiments [76–78].

In conclusion, to realize a structured environment with a giant atom, the analytical iFT method has the following problems:

(i) Too many coupling points might be needed, which is challenging for the experimental realization.

(ii) The remnant nonzero coupling in the band gaps is still high.

(iii) The coupling strengths alter their signs, which is unfeasible with the linear coupling elements used in the experiments.

B. Optimization method

To solve the above problems, we now present a general optimization algorithm to find the desired coupling sequence. Unlike previous setups using identical giant atom–photon interacting strength at each coupling point and equal distances between coupling points [25–27], our device relies on the optimal design of the coupling sequence.

We consider the unequal contribution of the modes with different unbalanced weights. For the band-gap environment, the coupling strength should be exactly zero inside the gap area, which is the most important feature for a band-gap environment. Outside the band-gap area, even if the interaction varies with k slightly (of the same order), the dynamics, such as trapped bound state and nonexponential decay led by band gaps, can still be observed. For the modes far away from the gap, strong coupling strengths does not affect the system's evolution due to large detuning relations. Therefore, the constraint requiring the k-space coupling strength outside the band gap to be identical is too strong. All these indicate that the desired k-space coupling can be obtained even when the real-space coupling strengths are of the same sign. Moreover, relaxing the restrict conditions by allowing G_k to vary with k can also reduce the required number of coupling points.

Now we convert realizing the target k-space coupling function as an optimization problem, which can be solved numerically. Given that the QED setup is constructed via conventional linear elements, the local phase $\theta(x_i) \equiv 0$, and $G_k^* = G_{-k}$ is valid. In this case, $\forall g(x_i) \geqslant 0$ should be added in the constraint conditions. The constraint conditions for this problems are summarized as follows:

1. $\forall g(x_i) \geqslant 0,$

2. $\eta\lambda_0 < \min\{x_{i+1} - x_i\},$

3. $-\dfrac{L}{2} < x_1 < x_N < \dfrac{L}{2}, \quad L \ll \bar{L}_0,$

4. $N \leqslant N_{\max},$ \hfill (11)

where $\bar{L}_0 = (\sum_i^N L_i)/N$ with L_i being the size of a decaying photonic wave packet from a small atom which just couples to the waveguide at a single point $g(x_i)$. Condition 1 restricts that all real-space coupling strengths are of the same sign, which avoids the coupling sign problem in QED setups with linear couplers.

Condition 2 sets the lower bound of the distance between two neighbor points. The reason for this restriction is that the coupling is mediated via physical elements with finite sizes (for example, capacitances or inductances in circuit QED). Due to fabrication limitation and to avoid crosstalk, two neighboring points cannot be too close to each other.

In condition 3, $\bar{L}_0$ is the average size of all the decaying wave packets. This restriction guarantees that the reabsorption and reemission of photons due to time retardation can be neglected.

Condition 4 sets the maximum coupling number, which is much smaller than that bounded by Eq. (8).

Considering a real-space sequence $g'(x_i)$ satisfying conditions 1–4, its k-space coupling function is denoted as $G'(k)$, which is obtained from Eq. (10). To find the optimized real-

space sequence, we define an objective function

$$C_m = \int_{-k_{\max}}^{k_{\max}} dk ||G'(k)| - |G^I(k)||w(k), \quad (12)$$

which can quantify the difference between obtained $G'(k)$ and the target coupling function. In Eq. (12) we introduce a weight function $w(k)$ to control the similarities for modes in different regimes. For simplicity, in this work we assume $w(k)$ to be

$$w(k) = \begin{cases} w_1, & \{k_0 - \frac{k_d}{2} < |k| < k_0 + \frac{k_d}{2}\}, \\ w_0, & \{k_0 + \frac{k_d}{2} < |k| < k_{\max}\}, \\ w_0, & \{-k_0 + \frac{k_d}{2} < k < k_0 - \frac{k_d}{2}\}. \end{cases} \quad (13)$$

Since the similarity between $G'(k)$ and $G^I(k)$ in the band-gap regime is much more important, we set $w_1 \gg w_0$ in Eq. (12). The optimization process minimizes C_m by searching the possible functions $g(x_i)$ satisfying the constraint condition in Eq. (11). Note that the constraint conditions stated in Eq. (11) can be different, depending on problems studied and experimental setups employed.

To simulate a band-gap environment, we set $k_d/k_0 = 1/15$, $L \simeq 17\lambda_0$, $\eta = 0.1\lambda_0$, $N_{\max} = 30$, and $w_1 = 60w_0$, and the obtained coupling sequence $g(x_i)$ (of the same sign) is listed in Table I of Appendix A. We employ the proposed optimization method by searching the sets $\{x_i, g(x_i)\}$. The optimized G_k is depicted in Fig. 4(a), and the enlarged plot around the band gap is in Fig. 4(b). We find that the number of points is reduced as $N = 28$, and the remnant nonzero coupling in gap area is decreased below $10^{-4}G_0$, which is much weaker than those in Fig. 2(c). Specially, G_k varies slightly with k for the modes outside the band gap, and the dc part (around $k \simeq 0$) will strongly couple to the giant atom because the $g(x_i)$'s signs are the same [see Fig. 4(a)]. To demonstrate the band-gap effect, the atomic frequency is usually set around ck_0, and therefore, the interaction with those low-frequency components is negligible due to large detuning effects, which can be verified from the numerical discussion in next section.

In experiments, reducing the number of coupling points can significantly simplify the whole setup. However, when N is too small, $G'(k)$ obtained by the proposed optimization algorithm will differ significantly from the target coupling function G_k. For example, when $N = 9$, we find $G'(k)$ unable to capture the important features of the band-gap environment, as shown in Fig. 4. Outside the band-gap area, the interaction strength begins to vary drastically. Moreover, the band gap obtained becomes much wider than the target coupling $G(k)$. Therefore, there is a lower bound for the coupling number in our proposal, below which the proposed algorithm cannot successfully find a suitable sequence.

We now summarize nontrivial differences between interferences in the photonic structure and giant atoms. First, photonic media are often fabricated with periodic structures to satisfy the Bragg reflection relation. However, in our proposal with giant atoms, the coupling points can distribute with unequal spacing, and the coupling amplitudes can also differ considerably (see Table I).

Second, in principle periodic photonic structures should be infinitely long (or at least much larger than the wavelength/wave-packet size); otherwise the photons will be

TABLE I. The real-space coupling sequence obtained via the optimized method proposed in this work. The corresponding k-space coupling is shown in Fig. 4(a).

position (x_i/λ_0)	−8.196	−7.901	−6.992	−6.682	−4.721	−4.396	−3.726	−3.419	−2.732	−2.441
coupling strength	0.0184	0.0291	0.0268	0.0146	0.0306	0.0502	0.0302	0.086	0.0317	0.1206
position (x_i/λ_0)	−1.71	−1.46	−0.507	−0.006	0.244	0.544	1.488	2.459	3.439	4.448
coupling strength	0.0906	0.0748	0.0223	0.1413	0.1553	0.9543	0.0458	0.1441	0.1305	0.1152
position (x_i/λ_0)	4.861	5.44	5.88	6.383	6.846	7.166	7.857	8.168		
coupling strength	0.0298	0.0393	0.0402	0.0219	0.0472	0.0184	0.0366	0.0265		

reflected by the boundary and the properties of structured environments cannot be observed. When configured as a quantum bus, the quantum coherence will inherently be destroyed by fabrication disorders along the long waveguide. For proposals with giant atoms, the coupling sequences are of finite length, with a finite number of couplings.

Those differences indicate that the interference mechanisms in those two paradigms are fundamentally different, even though the observed quantum optical phenomena are similar. Revealing the interference mechanism in giant atoms is of both fundamental and technological significance, which cannot follow the old routines used in photonic media.

III. QED IN BAND-GAP ENVIRONMENTS

A. Bound states

In Fig. 4(a), G_k is zero only in a narrow band with width k_d around $\pm k_0$; otherwise it remains a constant. This scenario is very similar to an atom interacting with a waveguide environment with band gaps in periodic structures. We now show that our setup shares very similar QED phenomena with conventional light-matter hybrid structures with photonic band gaps. Owing to suppression effects of the unbalanced weight function, the remnant coupling in the gap area is approximately zero, which can exactly mimic a band-gap environment.

We mainly focus on the fractional decay and bound state of the setup. In the single-excitation subspace, considering an initial excitation in the giant atom, the time-dependent state vector of the hybrid system is

$$|\psi(t)\rangle = \sum_k c_k(t)|g, 1_k\rangle + c_e(t)|e, 0\rangle.$$

The evolutions of the atomic population $|c_e(t)|^2$ are shown in Fig. 5(a) for different ω_q. There, $|c_e(t)|^2$ shows fractional decay with most energy being trapped inside the atom when ω_q is in the band gap. As discussed in Appendix A, the trapped population is approximately

$$|c_e(t \to \infty)|^2 \simeq \left(1 + \sum_k |G_k/\Delta_k|^2\right)^2.$$

Once ω_q is shifted far away from the gap area, $|c_e(t)|^2$ can exponentially decay to zero. Moreover, there exists a static bound state with its wave function localized around the atom. As derived in Appendix A, the real-space distribution for the photonic part of the bound state is

$$\psi_b(x) \propto \int_\infty^\infty dk \frac{G_k}{\Delta_k} e^{kx} = \sum_{i=1}^N \int_{-\infty}^\infty \frac{g(x_i)}{\Delta_k} e^{k(x-x_i)} dk. \quad (14)$$

In Fig. 5(b), we plot the field distribution by solving the system evolution to $\omega_c t = 1350$, which is well described by the stable bound state obtained in Eq. (14). All the above phenomena are very similar to those observed in setups with band-gap environments [51–55]. The counterintuitive phenomenon is that there is no stable bound state if a small
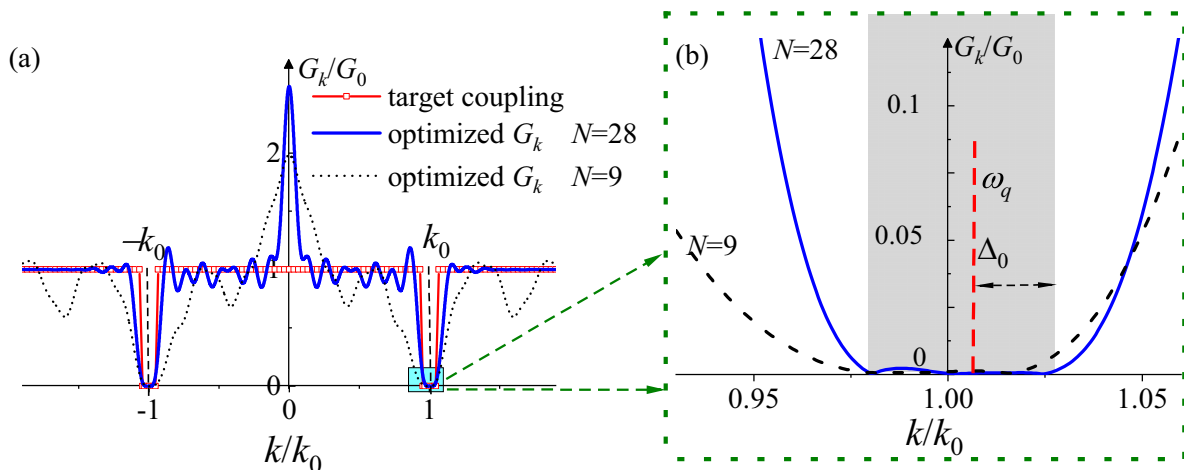

FIG. 4. (a) Coupling function G_k obtained via out optimization algorithm with $N = 28$ and $N = 9$. The real-space coupling sequence for $N = 28$ is listed in Table I of Appendix A. (b) The enlarged plot around k_0. The detuning between ω_q and the band edge of $N = 28$ is denoted as Δ_0.
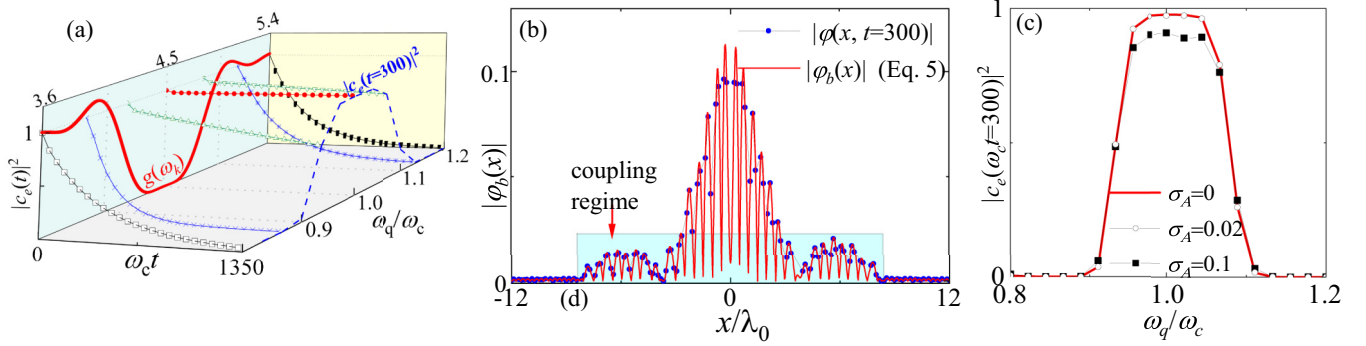
FIG. 5. (a) Time evolution of $|c_e(t)|^2$ for different atomic frequencies ω_q. (b) The photonic part of the bound state by setting $\omega_q = \omega_c$ (in the band gap). (c) In the presence of different disorder strengths, the trapped population $|c_e(t)|^2$ ($\omega_c t = 1350$) changes with ω_q.

atom is coupled to the conventional waveguide, while for giant atoms coupled to the waveguide, fields emitted from different coupling points interfere with each other [see Eq. (14)], which results in a time-independent $\phi_b(x)$. Note that in our discussion, the propagating time inside the giant atom is negligible. Since the waveguide supports only modes with nonzero group velocity, the wave packet outside the coupling regime cannot be reflected by any point and will propagate away. Therefore, $\phi_b(x)$ exactly lies within the coupling regime, which can be viewed as bound states in continuum studied in Refs. [11,26]. The structured environment supports modes with zero group velocity [52,55,73]; $\phi_b(x)$ can spread far away from the coupling point.

To include disorder effects, we sample the error $\delta g(x_i)$ randomly from a Gaussian distribution centered around zero with width $\sigma_A g(x_i)$. The simulation method is presented in Appendix B. We plot the disorder-averaged excitation being trapped inside the atom versus ω_q ($\omega_c t = 1350$), as shown in Fig. 5(c). The averaged coupling inside the gap becomes nonzero due to the random noise. Therefore, the protection from the band gap is destroyed, and $|c_e(t)|^2$ decays. The decoherence rate increases with growing σ_A, as shown in Fig. 5(c). However, for $\sigma_A < 0.1$, the evolution is only slightly affected by disorders. The experiments with giant emitters (with two or three coupling points) in Refs. [22,79] indicate that the amplitudes of the coupling sequence can be fabricated with a high accuracy. There is no fundamental limitation of increasing the coupling number to be tens of couplers. With the development of fabrication method, we believe that our proposal is within the capability of setups with giant atoms in the near future.

B. Dipole-dipole interactions

Considering multiple giant atoms coupled to a common waveguide with the optimized sequences for band-gap environments, these will interact with each other given that their bound states overlap with each other. We derive their dipole-dipole interaction strength by taking two giant atoms as an example. The Hamiltonian describing two giant atoms interacting with a common waveguide is expressed as

$$H_{\text{int2}} = \sum_k \Delta_k a_k^\dagger a_k + \sum_{i=1,2} \sum_k (G_{ki} a_k^\dagger \sigma_i^- + \text{H.c.}), \quad (15)$$

where we assume two atoms' transition frequencies to be identical, and $G_{ki} = \sum_j g_i(x_j) G_0 e^{-ikx_{ij}}$ is the coupling strength between giant atom i and the waveguide. For simplicity, the optimized coupling sequences of two atoms are assumed the same, i.e., $g_2(x_i) = g_1(x_i + d_s)$ with d_s being their separation distance. Given that their frequencies are in the band gap [see Fig. 4(b)], two atoms will exchange photons without decaying.

In principle, the exchange rate between two atoms can be tediously obtained by the standard resolvent-operator techniques [4]. This method is valid even when the atom-waveguide coupling enters into the strong-coupling regime. Here we focus on the weak-coupling regime, and the probability of photonic excitations in the waveguide is extremely low. In this case, the Rabi oscillating rate between two atoms corresponds to their interaction strength mediated by the waveguide's modes, which can be simply derived via the effective Hamiltonian method [80]. Only the modes outside the band gap interact with two atoms, and the dipole-dipole interacting Hamiltonian mediated by one mode k is derived as

$$H_{d-d,k} = \frac{G_{k1} G_{k2}^*}{\Delta_k} (\sigma_1^- a_k^\dagger \sigma_2^+ a_k - \sigma_2^+ a_k \sigma_1^- a_k^\dagger) + \text{H.c.} \quad (16)$$

The waveguide is just virtually excited and the photonic population is approximately zero. Therefore, by adopting the approximations $\langle a_k^\dagger a_k \rangle \simeq 0$ and $\langle a_k a_k^\dagger \rangle \simeq 1$, we can trace off the photonic freedoms in Eq. (16), and simplify Eq. (16) as

$$H_{d-d,k} \simeq -\frac{G_{k1} G_{k2}^*}{\Delta_k} \sigma_2^+ \sigma_1^- + \text{H.c.} \quad (17)$$

Note that the interaction Hamiltonian $H_{d-d,k}$ in Eq. (17) is only mediated by one mode k. By taking all the mode' contributions into account, we derive the total dipole-dipole interaction as

$$H_{d-d} = J_{AB}(\sigma_2^+ \sigma_1^- + \text{H.c.}), \quad (18)$$

with

$$J_{AB} = -\sum_k \frac{G_{k1} G_{k2}^*}{\Delta_k} = \frac{L_w}{2\pi} \int_{-k_{\max}}^{k_{\max}} \frac{|G_{k1}|^2 e^{ikd_s}}{\Delta_k} dk, \quad (19)$$

where $L_w \to \infty$ is the waveguide's length adopted in the numerical simulations, and we assume that the coupling sequence of atom b is the same with a, translated a distance
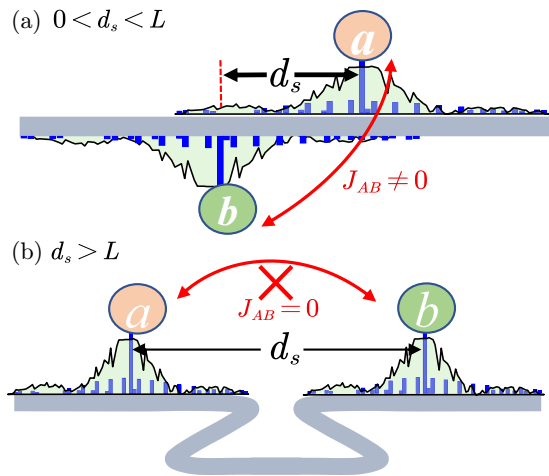
FIG. 6. A QED setup where two giant atoms a, b interact with the same waveguide. (b) When two atoms' bound states overlap with each other, their dipole-dipole exchange rate is nonzero. (b) Relative to (a), two giant atoms decouple with each other when their coupling regimes are separated.

d_s to a. A long waveguide is utilized to avoid photons being reflected by the boundary. Note that we adopt the translation relation between two coupling sequences, i.e., $G_{k2} = G_{k1}e^{-ikd_s}$. From Eq. (19), one can find that the coherent exchange channel is proportional to the overlap area between two bound states. Figure 7(a) depicts J_{AB} versus d_s [Eq. (19)], which matches well the numerical dynamical evolutions [obtained from the two atoms' Rabi oscillating frequency $2J_{AB}$; see Fig. 7(b)]. When ω_q lies in the band gap, due to the protection of the band gap effects, both collective and individual decays are zero. and the dipole-dipole exchange is free of decoherence. Since each bound state's distribution area coincides with the coupling regime, J_{AB} is nonzero only when two atoms' coupling regimes overlap with each other. The dipole-dipole interaction vanishes when d_s is larger than the coupling distance L ($L = 17\lambda_0$), as depicted in Fig. 6(b). We also consider two coupling sequences both experiencing independent disorders; the average Rabi oscillations are shown in Fig. 7(c). For $\sigma_A \simeq 0.02$, the decay of the exchange process is not apparent, and the two atoms can coherently exchange excitations with a high fidelity.

IV. BROADBAND CHIRAL EMISSION

In the above discussions, we assume that the coupling strengths $g(x_i)$ are real and of the same sign, which can be realized in experiments with linear QED elements. In this case, the k-space interaction satisfies $G_k = G_{-k}^*$, indicating that the spontaneous emission rates into the right ($k > 0$) and left directions ($k < 0$) are identical. Therefore, the photonic field along the waveguide has no chiral preference. Given that additional local phases are generated via synthetic methods, i.e., $g(x_i) = A(x_i)e^{i\theta(x_i)}$, the relation $|G_k| = |G_{-k}|$ is not valid again. In circuit QED this additional phase can be realized via nonlinear Josephson junctions. As demonstrated in Refs. [76,77,81], by applying a time-oscillating flux signal with phase $\theta(x_i)$ through the coupling loop at point x_i, the
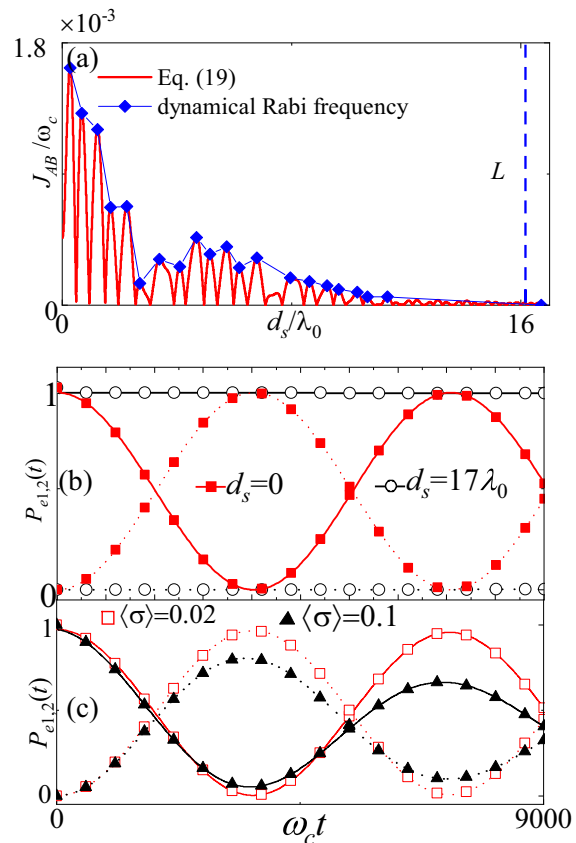

FIG. 7. (a) The dipole-dipole interaction strength vs the separation distance d_s ($\omega_q = 4.4$). (b) The Rabi oscillations for $d_s = 0$ and $d_s = 17\lambda_0 > L$, respectively. (c) The dissipative Rabi oscillations under different disorder strengths.

local phase $\theta(x_i)$ was successfully encoded into the coupling point.

To achieve chiral emission, the left-propagating modes should be decoupled from the giant atoms, a most important feature for G_k. Therefore, the weight function $w(k)$ inside the asymmetric gap is set to be much larger than outside the gap. Similar to realizing band-gap effects, we first define a target function:

$$G_k^I = \begin{cases} 0, & \{-k_0 - \frac{k_d}{2} < k < -k_0 + \frac{k_d}{2}\}, \\ G_0, & \{-k_{max} < k < -k_0 - \frac{k_d}{2}\}, \\ G_0, & \{-k_0 + \frac{k_d}{2} < k < k_{max}\}, \end{cases} \quad (20)$$

where the chiral bandwidth is k_d. We define a weight function during the optimizing process

$$w(k) = \begin{cases} w_1, & \{-k_0 - \frac{k_d}{2} < k < -k_0 + \frac{k_d}{2}\}, \\ w_0, & \{-k_{max} < k < -k_0 - \frac{k_d}{2}\}, \\ w_0, & \{-k_0 + \frac{k_d}{2} < k < k_{max}\}. \end{cases} \quad (21)$$

We optimize the target k-space interaction G_k^I with a wide asymmetric band gap (with a width $k_d/k_0 = 2/3$) centered at k_0, as shown in Fig. 8(a). We achieve $|G_k| \neq |G_{-k}|$ [16,82–84], indicating that chiral emission of photons can be observed [79,85–87]. To achieve the optimal sets $\{x_i, A(x_i), \theta(x_i)\}$, we choose the constraint conditions 2–4 of
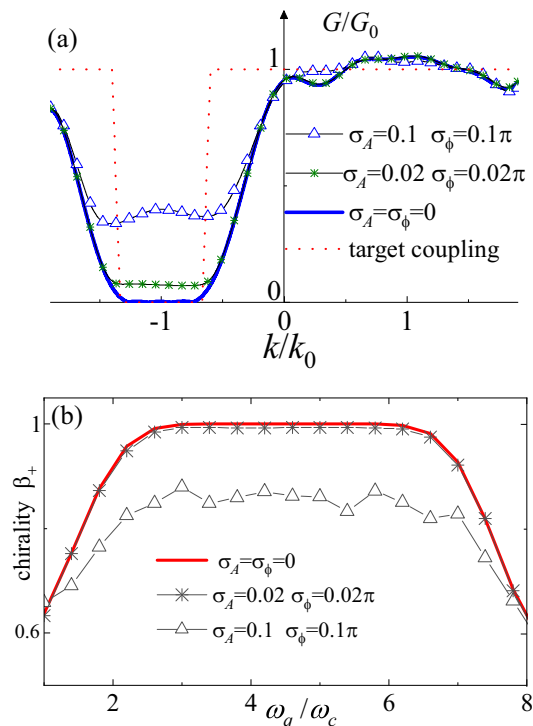
FIG. 8. (a) The averaged k-space coupling coefficient G_k for the sequence in Fig. 1 under different disorder strengths. (b) Chiral factor β_+ changes with ω_q in the presence of the disorder in (a).

Eq. (11). We search the optimized sequence by adopting $\eta = 0.125$, $N_{\max} = 8$, $w_1 = 30w_0$, and $L \simeq 2\lambda_0$. Similarly, searching the optimal sets $\{x_i, A(x_i), \theta(x_i)\}$ is now converted as a convex optimization problem by minimizing C_m.

Contrasting previous studies on chiral quantum optics targeting only on a single frequency [58,60], our proposed system can emit photons in a broadband frequency regime, given that the frequency of the giant atoms is freely tuned. The amplitudes $A(x_i)$ and phases $\theta(x_i)$ of the coupling sequence are listed in Table II. In contrast to photonic media with periodic structures, the coupling points are now distributed with unequal spacing, and their strengths differ considerably. Moreover, the total coupling number is $N = 10$ and the giant atom size is $L = x_N - x_1 < 2\lambda_0$, which is much shorter than in a structured photonic media. As depicted in Fig. 8(a), inside the asymmetric gap, the optimized G_k is approximately zero, and matches the target coupling function. Compared to realizing chiral emission from a pair of entangled emitters [88], the Lorentz reciprocity in our proposed setup is broken. Moreover, chiral emissions in our proposal do not need any preparation of fragile entangled states, and therefore are more robust to decoherence noise. The chiral factor $\beta_\pm$ can be

derived by employing the Weisskopf-Wigner theory

$$\beta_\pm = \frac{|G_{\pm k_r}|^2}{|G_{k_r}|^2 + |G_{-k_r}|^2}, \tag{22}$$

where $k_r = \omega_q/c$, $G_{\pm k_r}$ are the coupling strengths at the resonant positions, and $+ (-)$ corresponds to the right (left) propagating mode. The asymmetric coupling with $G_{k_r} \gg G_{-k_r}$ indicates a right chiral emission. Moreover, the asymmetric regime is very wide [see Fig. 8(b)], indicating a broadband chiral emission for frequency-tunable giant emitters.

When ω_q varies in a wide frequency regime, the chiral factor always approaches $\beta_+ \simeq 1$. Such broadband chiral behavior for frequency-tunable giant emitters has not yet been reported in other quantum setups. For example, the chiral bandwidth of nanophotonic structures is equal to the Lorentzian transmission width of the emitter, which is much narrower than that in our proposal [64]. In strongly confined nanophotonic structures, the chirality is linked to spin-momentum locking, while the chiral emission in our proposal is based on interference effects. This is another fundamental advantage of our proposal.

For the experimental realization of our setup, the fabrication errors can perturb the optimized coupling sequence. To include this disorder effect, we add random perturbations to the coupling strength as (see discussion in Appendix B)

$$g(x_i) \to [A(x_i) + \delta A(x_i)]e^{i[\theta(x_i) + \delta\theta(x_i)]}.$$

The random offsets are sampled from Gaussian distributions with amplitude (phase) disorder width $\sigma_\alpha A(x_i)$ (σ_ϕ). We plot the disorder-averaged k-space coupling for different $\{\sigma_A, \sigma_\phi\}$, as shown in Fig. 8(a). The asymmetric band gap is lifted due to disorders. The evolution shows that the chiral factor is approximately 1 in a very wide frequency range for disorder strengths $\{\sigma_A = 0.02, \sigma_\phi = 0.02\pi\}$ [see Fig. 8(b)]. Even with stronger disorders, i.e., $\{\sigma_A = 0.1, \sigma_\phi = 0.1\pi\}$, the chirality remains above 0.85, indicating that the broadband chiral emission realized in our proposal is robust to fabrication errors in the coupling sequence.

V. CONCLUSION

In this work, we explore the possibilities to realize quantum optics in structured photonic environments with giant atoms. We show that most phenomena can be reproduced by designing the couplings between giant atoms and conventional environments without any nanostructure. We first introduce a general method to find the optimized coupling sequences for arbitrarily structured light-matter interaction. Given that a position-dependent phase is added to each coupling point, the giant atom can chirally emit photons in a very wide frequency regime, which has no analog in other quantum setups. We also show that the quantum effects in a band-gap environ-

TABLE II. The amplitudes and phases of the coupling sequence in Fig. 7, which is obtained via the proposed optimization method.

position (x_i/λ_0)	-0.909	-0.757	-0.383	-0.508	-0.0975	-0.222	0.393	0.120	0.641	0.909
amplitude $A(x_i)$	0.088	0.130	0.628	0.429	0.392	0.591	0.365	0.198	0.615	0.243
phase $\theta(x_i)$	0.388π	-0.500π	-0.446π	0.500π	-0.500π	0.500π	-0.500π	0.179π	0.0048π	0.460π

ment (such as atomic fractional decay, static bound state, and nondissipative dipole-dipole interactions) can all be observed. Numerical results indicate that all the above QED phenomena can be observed even in the presence of fabrication disorder in coupling sequences. Our proposed methods are very general and can also realize other types of structured environments, e.g., with multiple band gaps or a narrow spectrum bandwidth. Other quantum effects in those artificial environments, such as non-Markovian dynamics or multiphoton processes, can also be revisited [89–92], and new quantum effects might be observed.

APPENDIX A: FRACTIONAL DECAY AND BOUND STATES

We first estimate the size of the decaying wave packet for a single coupling point. According to the Weisskopf-Wigner theory, given that a small-atom coupling at point x_i, the decay rate, and the corresponding wave packet size are respectively derived as

$$\Gamma_i = \frac{2\pi |g'_{x_i}|^2}{c}, \quad g'_{x_i} = g(x_i)\sqrt{\frac{L_w}{2\pi}}, \quad L_i \simeq 2c\Gamma_i^{-1}, \quad \text{(A1)}$$

the coupling constant is set as $G_0 = 0.002\omega_c$ in our discussion. In numerical simulations, the mode number in the regime $-k_{\max} < k < k_{\max}$ is discretized with an interval $\delta k = 0.67 \times 10^{-3}k_0$, which is equal to considering a waveguide with length $L_w = 1.5 \times 10^3 \lambda_0$. Such a long waveguide guarantees the propagating wave packet never touches the boundary. By employing the coupling sequence in Table I, the maximum and average sizes of the wave packet are respectively calculated as $\max\{L_i\} \simeq 2 \times 10^2 \lambda_0$ and $\bar{L}_0 \simeq 8 \times 10^4 \lambda_0$, which are both much larger than the giant atom's size L. Therefore, we can neglect the time retardation effects.

Assuming a single excitation initially trapped inside the giant atom, the system's state at time t is expanded as $|\psi(t)\rangle = \sum_k c_k(t)|g, 1_k\rangle + c_e(t)|e, 0\rangle$. The dynamical evolution is numerically solved in this single-excitation subspace by discretizing the waveguide's modes in k space. A similar method can be found in Ref. [16]. We start from the evolution

governed by the interaction Hamiltonian in Eq. (1), which is derived as

$$\dot{c}_e(t) = -i \sum_k G_k c_k(t), \quad \text{(A2)}$$

$$\dot{c}_k(t) = -i\Delta_k c_k(t) - iG_k^* c_e(t). \quad \text{(A3)}$$

The above equations can be expressed in Laplace space as

$$s\tilde{c}_e(s) - c_e(t_0) = -i \sum_k G_k \tilde{c}_k(s), \quad \text{(A4)}$$

$$s\tilde{c}_k(s) - c_k(t_0) = -i\Delta_k \tilde{c}_k(s) - iG_k^* \tilde{c}_e(s), \quad \text{(A5)}$$

and the initial conditions are $c_k(t=0) = 0$ and $c_e(t=0) = 1$. The time-dependent evolution is derived by the inverse Laplace transformation [82]

$$c_e(t) = \frac{1}{2\pi i} \lim_{E \to \infty} \int_{\epsilon - iE}^{\epsilon + iE} \tilde{c}_e(s)e^{st}ds, \quad \epsilon > 0. \quad \text{(A6)}$$

Finally, we obtain

$$\tilde{c}_e(s) = \frac{1}{s - \Sigma_e(s)}, \quad \Sigma_e(s) = \sum_k \frac{-|G_k|^2}{s + i\Delta_k}, \quad \text{(A7)}$$

where $\Sigma_e(s)$ is the self-energy of the giant atom. Given that the atomic frequency is in the gap area, part of the energy will be trapped inside the giant atom since there is no resonant pathway to radiate the excitation away. This point can also be verified from the roots of the transcendental equation $s - \Sigma_e(s) = 0$, which correspond to the intersection points of $f(s) = s$ and $f(s) = \Sigma_e(s)$ [see Fig. 9(a)]. We find that there is only *one* purely imaginary solution s_0 (blue dots), which increases with G_0. Since s_0 is the imaginary pole for $\tilde{c}_e(s)$, it corresponds to a static bound state which does not decay with time [4]. In this scenario, part of the atomic energy will be trapped without decaying, and the steady amplitude of $c_e(t)$ can be obtained via the residue theorem

$$c_e(t \to \infty) = \text{Res}(s_0) = \frac{1}{1 - \partial_s \Sigma_e(s)}\bigg|_{s=s_0}$$

$$= \frac{1}{1 - \sum_k \frac{|G_k|^2}{(s_0 + i\Delta_k)^2}}. \quad \text{(A8)}$$

In Fig. 9(b), we plot $|c_e(t \to \infty)|^2$ versus the coupling strength G_0, which matches well with $|\text{Res}(s_0)|^2$. Given that the coupling strength is weak, most of the energy was trapped inside the atom, and the steady-state population is $|c_e(t \to \infty)|^2 \simeq 1$. When increasing G_0, the trapped atomic excitation will decrease, and more energy will distribute on the waveguide.

We now show that the partial photonic field is trapped inside the coupling area without propagating away, which is akin to the bound state in QED setups with band-gap media. The bound state, which is the eigenstate of the system Hamiltonian, can be obtained by solving the following Schrödinger equation $H_{\text{int}}|\psi_b\rangle = E_b|\psi_b\rangle$, where $|\psi_b\rangle = \cos(\theta)|e, 0\rangle + \sin\theta \sum_k c_k|g, 1_k\rangle$, with θ being the mixing angle. The solution is obtained from the following equations:

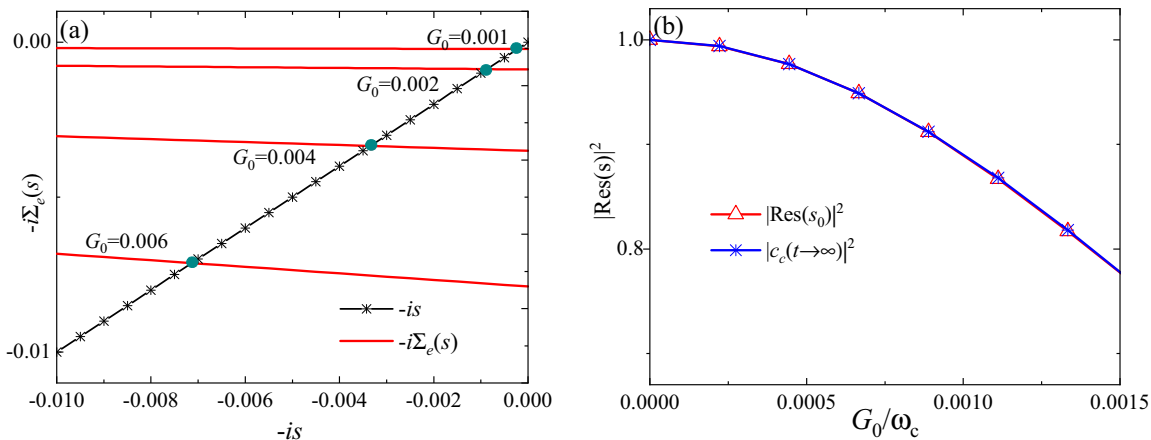$$c_k = \frac{G_k}{\tan\theta(E_b - \Delta_k)}, \quad \text{(A9)}$$

FIG. 9. (a) The root of transcendental equation $s - \Sigma_e(s) = 0$ can be numerically solved, which corresponds to the intersection point (blue dots) for different values of G_0. (b) The excitation population trapped inside the atom $|\text{Res}(s_0)|^2$ changes with G_0 [calculated via the residue theorem in Eq. (A8)], and matches well the dynamical evolution $|c_e(t \to \infty)|^2$. The atomic frequency is fixed at $\omega_q = \omega_c$.

$$E_b = \sum_k \frac{|G_k|^2}{E_b - \Delta_k}, \tag{A10}$$

$$\tan \theta = \sum_k \frac{|G_k|^2}{(E_b - \Delta_k)^2}. \tag{A11}$$

Note that Eq. (A10) is the same with Eq. (A7) (by replacing E_b with is_0). In our discussion, the interaction between the giant atom and the waveguide is weak. Therefore, the eigenenergy E_b is around zero [i.e., $s_0 \simeq 0$; see Fig. 9(a)]. Under this condition, most of the energy will be trapped inside the atom, and the mixed angle $\theta \simeq 0$. Employing the approximations $\sin \theta \simeq \tan \theta$ and $E_b \simeq 0$, the photonic field is derived as

$$\psi_b(x) = \frac{\sin \theta}{\sqrt{L_w}} \sum_k c_k e^{kx} \simeq -\frac{\sqrt{L_w}}{2\pi} \int_{-\infty}^{\infty} \frac{G_k}{\Delta_k} e^{kx} dk. \tag{A12}$$

By substituting the real-space coupling in Eq. (10) into $\psi(x)$, we rewrite $\psi_b(x)$ as

$$\psi_b(x) = -\frac{\sqrt{L}}{2\pi} \sum_{x_i} \phi_{bi}(x),$$

$$\phi_{bi}(x) = \int_{-\infty}^{\infty} \frac{g(x_i)}{\omega_k - \omega_q} e^{k(x-x_i)} dk. \tag{A13}$$

In Eq. (A13), $\phi_{bi}(x)$ is induced by a small atom which couples to the 1D waveguide at the single point x_i. In the weak-coupling regime, the small atom will exponentially decay all its energy into the waveguide given that $t \to \infty$. Therefore, there is no stable bound state for a small atom, which can also be explained by the behavior of $\psi_{bi}(x)$ in Eq. (A13), where

$$\lim_{\omega_k \to \omega_q} \frac{g(x_i) e^{-ikx_i}}{\omega_k - \omega_q} = \infty \tag{A14}$$

is divergent. That is, the expression for $\phi_{bi}(x)$ is nonintegrable.

The counterintuitive result is that a stable bound state appears when all the coupling points act simultaneously. The interference between different points prevents the giant atom

from decaying, and results in a static bound state even when its frequency lies inside the continuum spectrum.

APPENDIX B: SIMULATING DISORDER EFFECTS

1. Disorder effects in band-gap environments

When implementing the optimal coupling sequences in experiments, there will be fabrication errors in both coupling positions and amplitudes. Next we evaluate their effects by considering circuit-QED with a transmon qubit [with frequency $\omega_q/(2\pi) = 3\,\text{GHz}$, for example]. The phase velocity along the transmission-line waveguide is set as $c = 2 \times 10^8\,\text{m/s}$. Therefore, the wavelength is $\lambda_0 \simeq 7 \times 10^{-2}\,\text{m}$. We first investigate the disorder in positions by adding random offsets to the coupling sequence, i.e., $g(x_i) \to g(x_i + \delta x_i)$. Here δx_i is sampled from a Gaussian distribution centered around zero and with a width σ_P.

Consequently, the average k-space coupling function is defined as

$$\bar{G}_k = \frac{1}{N_{\text{dis}}} \sum_{n=1}^{N_{\text{dis}}} \sum_{x_i} g(x_i + \delta x_i) e^{-ik(x_i + \delta x_i)}, \tag{B1}$$

where N_{dis} is the number of disorder realizations in the numerical simulations. In our discussion, we set $N_{\text{dis}} = 200$, which is large enough for the errors considered in this work. To investigate the disorder effects on the quantum dynamics, we numerically simulate the evolution by taking the average of all the realizations. We define the disorder-averaged population as

$$\bar{p}_e(t) = \frac{1}{N_{\text{dis}}} \sum_{n=1}^{N_{\text{dis}}} |c_e(t)|^2. \tag{B2}$$

In Fig. 10(a), we plot $\bar{G}_k$ for different disorder strengths, and find that the band gap is lifted higher than zero. Given that $\sigma_P = 0.001\lambda_0 \simeq 0.07\,\text{mm}$, the coupling strength in the band gap is around zero, and the giant atom is still protected from decaying [see Fig. 10(b)]. Only when the location error is $\sigma_P > 0.01\lambda_0 \simeq 0.7\,\text{mm}$ (which should already be visible to
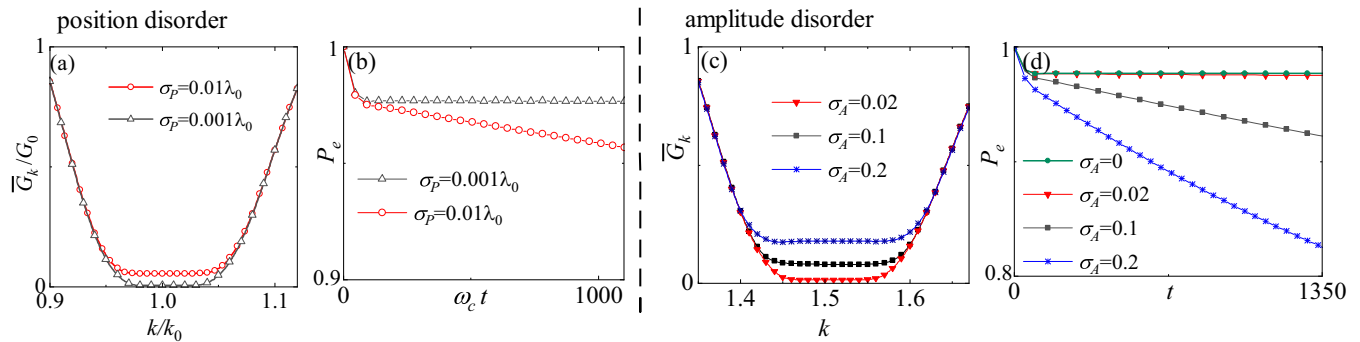
FIG. 10. (a), (c) The average k-space coupling $\bar{G}_k$ in the band-gap regime under different position and amplitude disorders, respectively. The disorder-averaged population $|\bar{p}_e(t)|$ changes with time are shown in (b) and (d). In each realization the random offsets are added into the optimal coupling sequence in Table I. Here we set $\omega_q = \omega_c$, and the other parameters are the same as those in Fig. 5(a).

the naked eye), the band gap will be lifted around $\bar{G}_k \simeq 0.05$ and the transmon will gradually decay due to the position disorders. Current and future experiments on circuit QED can locate coupling elements with accuracy higher than $0.01\lambda_0$. Therefore, we can neglect the position errors in our discussion.

Next we consider random offsets to the amplitude coupling sequence, i.e., $g(x_i) \to g(x_i) + \delta g(x_i)$. Here $\delta g(x_i)$ is sampled from a Gaussian distribution centered around zero and with a width $\sigma_A g(x_i)$. In Fig. 10(c), we plot $\bar{G}_k$ for different disorder strengths, and find that the band gap is lifted higher than zero. The trapped excitation inside the atom becomes unstable and will slowly leak into the waveguide [see Fig. 10(d)]. The decoherence rate led by disorder increases with disorder strengths. It can be inferred that when $\sigma_A > 0.2$, the protection effects of the band gap will be swamped by the disorder noise.

2. Disorder effects in broadband chiral emission

The obtained optimal set $\{x_i, A(x_i), \theta(x_i)\}$ for broadband chiral emission is listed in Table II and plotted in Fig. 1. We now consider that the coupling strength at each point experiences disorders in both its amplitude and phase, i.e.,

$$g(x_i) \to [A(x_i) + \delta A(x_i)] \exp[i\theta(x_i) + i\delta\theta(x_i)].$$

Both the amplitude and phase disorders are assumed to satisfy a Gaussian distribution centered around zero. The amplitude disorder widths σ_A are proportional to the local strength $A(x_i)$, while the phase disorder widths σ_ϕ are assumed identical for all the coupling points. We plot the disorder averaged k-space coupling function in Fig. 8(a). We find that the disorder does not affect the coupling strength too much for the modes outside the chiral regime. Inside the asymmetric band gap, the zero coupling will be lifted higher than zero with stronger disorder strengths.

To show how disorder disturbs the chiral emission, we numerically simulate disorder-averaged evolutions by defining the photonic field as

$$\bar{\Psi}_\gamma(x,t) = \frac{1}{N_{\mathrm{dis}}} \sum_{n=1}^{N_{\mathrm{dis.}}} |\psi_\gamma(x,t)|^2, \tag{B3}$$

$$\psi_\gamma(x,t) \propto \int_{-\infty}^{\infty} dk\, c_k(t) e^{-ikx}. \tag{B4}$$

In Figs. 11(a)–11(c), we plot how the disorder-averaged field distribution $\psi_\gamma(x,t)$ changes with time in the presence of $\{\sigma_A, \sigma_\phi\}$. When the coupling disorders are as strong as $\{\sigma_A = 0.1g(x_i), \sigma_\phi = 0.1\pi\}$, most of the photonic field still decays to the right of the waveguide. To evaluate the chiral behavior of our proposal, we define the chiral factor as

$$\beta_\pm = \frac{\Phi_{R(L)}}{\Phi_R + \Phi_L}, \tag{B5}$$

$$\Phi_{R/L} = \frac{1}{N_{\mathrm{dis}}} \sum_{\mathrm{dis.}} \lim_{t\to\infty} \left| \int_0^{\pm\infty} |\psi_\gamma(x',t)|^2 dx' \right|. \tag{B6}$$

Employing the above methods and definitions, we plot Fig. 8, which shows that our proposal can chirally route photons in a broadband range even in the presence of strong disorder.

There are many types of layouts which can encode the required phases via nonlinear couplings. For example, by applying a time-dependent flux through a coupler loop at position x_i, the coupling strength can be written as

$$g(x_i, t) = g_i \frac{\Phi_{\mathrm{ext}}}{\Phi_0} \cos(\Omega_d t + \phi_i), \tag{B7}$$

where g_i is the coupling constant depending on the circuit parameters (such as the Josephson inductance and loop inductance), Φ_{ext} (Ω_d) is the time-dependent driving amplitude (frequency), and ϕ_i is the phase to be encoded at x_i. Therefore, we do not require the circuit parameters to be fabricated to a certain value. If g_i is smaller (larger) than the required value, the external driving amplitude Φ_{ext} can be increased (decreased) accordingly when calibrating the whole setup. Therefore, the disorder is affected by the drive, which is usually the output from devices such as arbitrary function generators [95]. In many labs, both the amplitude and phase of the drive can be controlled with high accuracy, indicating that the disorder in the nonlinear coupling layout can be suppressed to low values in experiments.
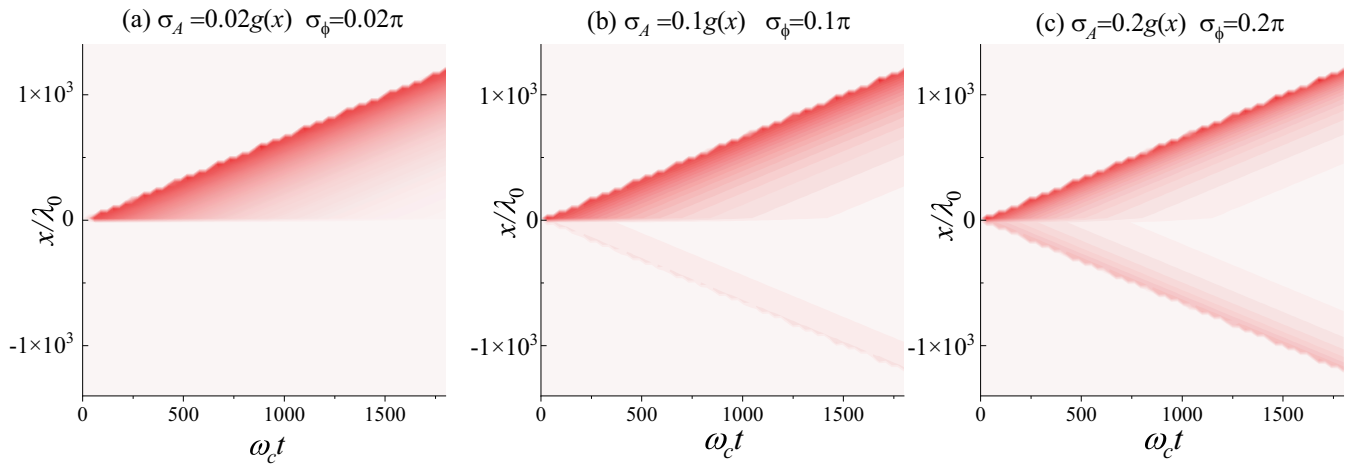
FIG. 11. (a)–(c) Time evolution of the chiral field distributions for various disorder strengths. The atomic frequency is fixed at $\omega_q = \omega_c$.

[1] M. O. Scully and M. S. Zubairy, *Quantum Optics* (Cambridge University Press, Cambridge, UK, 1997).

[2] G. S. Agarwal, *Quantum Optics* (Cambridge University Press, Cambridge UK, 2012).

[3] H. J. Kimble, M. Dagenais, and L. Mandel, Photon antibunching in resonance fluorescence, Phys. Rev. Lett. **39**, 691 (1977).

[4] C. Cohen-Tannoudji, J. Dupont-Roc, and G. Grynberg, *Atom-Photon Interactions* (Wiley, Weinheim Germany, 1998).

[5] X. Gu, A. F. Kockum, A. Miranowicz, Y.-X. Liu, and F. Nori, Microwave photonics with superconducting quantum circuits, Phys. Rep. **718-719**, 1 (2017).

[6] A. F. Kockum, A. Miranowicz, S. De Liberato, S. Savasta, and F. Nori, Ultrastrong coupling between light and matter, Nat. Rev. Phys. **1**, 19 (2019).

[7] M. V. Gustafsson, T. Aref, A. F. Kockum, M. K. Ekstrom, G. Johansson, and P. Delsing, Propagating phonons coupled to an artificial atom, Science **346**, 207 (2014).

[8] A. Frisk Kockum, P. Delsing, and G. Johansson, Designing frequency-dependent relaxation rates and Lamb shifts for a giant artificial atom, Phys. Rev. A **90**, 013837 (2014).

[9] G. Andersson, B. Suri, L. Guo, T. Aref, and P. Delsing, Non-exponential decay of a giant artificial atom, Nat. Phys. **15**, 1123 (2019).

[10] W. Zhao and Z. Wang, Single-photon scattering and bound states in an atom-waveguide system with two or multiple coupling points, Phys. Rev. A **101**, 053855 (2020).

[11] S. Guo, Y. Wang, T. Purdy, and J. Taylor, Beyond spontaneous emission: Giant atom bounded in the continuum, Phys. Rev. A **102**, 033706 (2020).

[12] L. Du, M.-R. Cai, J.-H. Wu, Z.-H. Wang, and Y. Li, Single-photon nonreciprocal excitation transfer with non-Markovian retarded effects, Phys. Rev. A **103**, 053701 (2021).

[13] A. Soro and A. F. Kockum, Chiral quantum optics with giant atoms, Phys. Rev. A **105**, 023712 (2022).

[14] X.-L. Yin, Y.-H. Liu, J.-F. Huang, and J.-Q. Liao, Single-photon scattering in a giant-molecule waveguide-QED system, Phys. Rev. A **106**, 013715 (2022).

[15] L. Du, Y. Zhang, J.-H. Wu, A. F. Kockum, and Y. Li, Giant atoms in a synthetic frequency dimension, Phys. Rev. Lett. **128**, 223602 (2022).

[16] X. Wang and H.-R. Li, Chiral quantum network with giant atoms, Quantum Sci. Technol. **7**, 035007 (2022).

[17] H. Xiao, L. Wang, Z.-H. Li, X. Chen, and L. Yuan, Bound state in a giant atom-modulated resonators system, npj Quantum Inf. **8**, 80 (2022).

[18] W. Cheng, Z. Wang, and Y.-X. Liu, Topology and retardation effect of a giant atom in a topological waveguide, Phys. Rev. A **106**, 033522 (2022).

[19] Q.-Y. Qiu, Y. Wu, and X.-Y. Lü, Collective radiance of giant atoms in non-Markovian regime, Sci. China Phys. Mech. **66**, 224212 (2023).

[20] W. Z. Jia and M. T. Yu, Atom-photon dressed states in a waveguide-QED system with multiple giant atoms coupled to a resonator-array waveguide, arXiv:2304.02072.

[21] A. C. Santos and R. Bachelard, Generation of maximally entangled long-lived states with giant atoms in a waveguide, Phys. Rev. Lett. **130**, 053601 (2023).

[22] B. Kannan *et al.*, Waveguide quantum electrodynamics with superconducting artificial giant atoms, Nature (London) **583**, 775 (2020).

[23] L.-Z. Guo, A. Grimsmo, A. F. Kockum, M. Pletyukhov, and G. Johansson, Giant acoustic atom: A single quantum system with a deterministic time delay, Phys. Rev. A **95**, 053821 (2017).

[24] X. Wang, T. Liu, A. F. Kockum, H.-R. Li, and F. Nori, Tunable chiral bound states with giant atoms, Phys. Rev. Lett. **126**, 043602 (2021).

[25] A. F. Kockum, G. Johansson, and F. Nori, Decoherence-free interaction between giant atoms in waveguide quantum electrodynamics, Phys. Rev. Lett. **120**, 140404 (2018).

[26] L.-Z. Guo, A. F. Kockum, F. Marquardt, and G. Johansson, Oscillating bound states for a giant atom, Phys. Rev. Res. **2**, 043014 (2020).

[27] K. Lim, W.-K. Mok, and L.-C. Kwek, Oscillating bound states in non-Markovian photonic lattices, Phys. Rev. A **107**, 023716 (2023).

[28] P. Lodahl, S. Mahmoodian, and S. Stobbe, Interfacing single photons and single quantum dots with photonic nanostructures, Rev. Mod. Phys. **87**, 347 (2015).

[29] A. Goban, C.-L. Hung, J. D. Hood, S.-P. Yu, J. A. Muniz, O. Painter, and H. J. Kimble, Superradiance for atoms trapped along a photonic crystal waveguide, Phys. Rev. Lett. **115**, 063601 (2015).

[30] D. Roy, C. M. Wilson, and O. Firstenberg, Colloquium: Strongly interacting photons in one-dimensional continuum, Rev. Mod. Phys. **89**, 021001 (2017).

[31] D. E. Chang, J. S. Douglas, A. González-Tudela, C.-L. Hung, and H. J. Kimble, Colloquium: Quantum matter built from nanoscopic lattices of atoms and photons, Rev. Mod. Phys. **90**, 031002 (2018).

[32] S.-P. Yu, J. A. Muniz, C.-L. Hung, and H. J. Kimble, Two-dimensional photonic crystals for engineering atom-light interactions, Proc. Natl. Acad. Sci. USA **116**, 12743 (2019).

[33] M. Scigliuzzo, G. Calajò, F. Ciccarello, D. Perez Lozano, A. Bengtsson, P. Scarlino, A. Wallraff, D. Chang, P. Delsing, and S. Gasparinetti, Controlling atom-photon bound states in an array of Josephson-junction resonators, Phys. Rev. X **12**, 031036 (2022).

[34] J.-S. Tang, W. Nie, L. Tang, M.-Y. Chen, X. Su, Y.-Q. Lu, F. Nori, and K.-Y. Xia, Nonreciprocal single-photon band structure, Phys. Rev. Lett. **128**, 203602 (2022).

[35] A. Kofman, G. Kurizki, and B. Sherman, Spontaneous and induced atomic decay in photonic band structures, J. Mod. Opt. **41**, 353 (1994).

[36] D. R. Smith, W. J. Padilla, D. C. Vier, S. C. Nemat-Nasser, and S. Schultz, Composite medium with simultaneously negative permeability and permittivity, Phys. Rev. Lett. **84**, 4184 (2000).

[37] P. Lambropoulos, G. M. Nikolopoulos, T. R. Nielsen, and S. Bay, Fundamental quantum optics in structured reservoirs, Rep. Prog. Phys. **63**, 455 (2000).

[38] M. Kafesaki, I. Tsiapa, N. Katsarakis, T. Koschny, C. M. Soukoulis, and E. N. Economou, Left-handed metamaterials: The fishnet structure and its variations, Phys. Rev. B **75**, 235114 (2007).

[39] D. Lu, J. J. Kan, E. E. Fullerton, and Z. Liu, Enhancing spontaneous emission rates of molecules using nanopatterned multilayer hyperbolic metamaterials, Nat. Nanotechnol. **9**, 48 (2014).

[40] S. Indrajeet, H. Wang, M. D. Hutchings, B. G. Taketani, F. K. Wilhelm, M. D. LaHaye, and B. L. T. Plourde, Coupling a superconducting qubit to a left-handed metamaterial resonator, Phys. Rev. Appl. **14**, 064033 (2020).

[41] M. Stewart, J. Kwon, A. Lanuza, and D. Schneble, Dynamics of matter-wave quantum emitters in a structured vacuum, Phys. Rev. Res. **2**, 043307 (2020).

[42] S. John and J. Wang, Quantum electrodynamics near a photonic band gap: Photon bound states and dressed atoms, Phys. Rev. Lett. **64**, 2418 (1990).

[43] F. Le Kien, V. I. Balykin, and K. Hakuta, Atom trap and waveguide using a two-color evanescent light field around a subwavelength-diameter optical fiber, Phys. Rev. A **70**, 063403 (2004).

[44] F. Le Kien, S. Dutta Gupta, V. I. Balykin, and K. Hakuta, Spontaneous emission of a cesium atom near a nanofiber: Efficient coupling of light to guided modes, Phys. Rev. A **72**, 032509 (2005).

[45] E. Vetsch, D. Reitz, G. Sagué, R. Schmidt, S. T. Dawkins, and A. Rauschenbeutel, Optical interface created by laser-cooled atoms trapped in the evanescent field surrounding an optical nanofiber, Phys. Rev. Lett. **104**, 203603 (2010).

[46] C. L. Hung, S. M. Meenehan, D. E. Chang, O. Painter, and H. J. Kimble, Trapped atoms in one-dimensional photonic crystals, New J. Phys. **15**, 083026 (2013).

[47] N. V. Corzo, B. Gouraud, A. Chandra, A. Goban, A. S. Sheremet, D. V. Kupriyanov, and J. Laurat, Large Bragg reflection from one-dimensional chains of trapped atoms near a nanoscale waveguide, Phys. Rev. Lett. **117**, 133603 (2016).

[48] Y. B. Liu and A. A. Houck, Quantum electrodynamics near a photonic bandgap, Nat. Phys. **13**, 48 (2017).

[49] L. Zhou, Z. R. Gong, Y.-X. Liu, C. P. Sun, and F. Nori, Controllable scattering of a single photon inside a one-dimensional resonator waveguide, Phys. Rev. Lett. **101**, 100501 (2008).

[50] J.-Q. Liao, Z. R. Gong, L. Zhou, Y.-X. Liu, C. P. Sun, and F. Nori, Controlling the transport of single photons by tuning the frequency of either one or two cavities in an array of coupled cavities, Phys. Rev. A **81**, 042304 (2010).

[51] A. Goban, C.-L. Hung, S.-P. Yu, J. D. Hood, J. A. Muniz, J. H. Lee, M. J. Martin, A. C. McClung, K. S. Choi, D. E. Chang, O. Painter, and H. Kimble, Atom-light interactions in photonic crystals, Nat. Commun. **5**, 3808 (2014).

[52] J. S. Douglas, H. Habibian, C.-L. Hung, A. V. Gorshkov, H. J. Kimble, and D. E. Chang, Quantum many-body models with cold atoms coupled to photonic crystals, Nat. Photon. **9**, 326 (2015).

[53] J. S. Douglas, T. Caneva, and D. E. Chang, Photon molecules in atomic gases trapped near photonic crystal waveguides, Phys. Rev. X **6**, 031017 (2016).

[54] J. D. Hood, A. Goban, A. Asenjo-Garcia, M. Lu, S.-P. Yu, D. E. Chang, and H. J. Kimble, Atom-atom interactions around the band edge of a photonic crystal waveguide, Proc. Natl. Acad. Sci. USA **113**, 10507 (2016).

[55] A. González-Tudela, C.-L. Hung, D. E. Chang, J. I. Cirac, and H. J. Kimble, Subwavelength vacuum lattices and atom-atom interactions in two-dimensional photonic crystals, Nat. Photon. **9**, 320 (2015).

[56] E. Munro, L. C. Kwek, and D. E. Chang, Optical properties of an atomic ensemble coupled to a band edge of a photonic crystal waveguide, New J. Phys. **19**, 083018 (2017).

[57] L. Leonforte, A. Carollo, and F. Ciccarello, Vacancy-like dressed states in topological waveguide QED, Phys. Rev. Lett. **126**, 063601 (2021).

[58] R. Mitsch, C. Sayrin, B. Albrecht, P. Schneeweiss, and A. Rauschenbeutel, Quantum state-controlled directional spontaneous emission of photons into a nanophotonic waveguide, Nat. Commun. **5**, 5713 (2014).

[59] K. Y. Bliokh, D. Smirnova, and F. Nori, Quantum spin Hall effect of light, Science **348**, 1448 (2015).

[60] J. Petersen, J. Volz, and A. Rauschenbeutel, Chiral nanophotonic waveguide interface based on spin-orbit interaction of light, Science **346**, 67 (2014).

[61] A. B. Young, A. C. T. Thijssen, D. M. Beggs, P. Androvitsaneas, L. Kuipers, J. G. Rarity, S. Hughes, and R. Oulton, Polarization engineering in photonic crystal waveguides for spin-photon entanglers, Phys. Rev. Lett. **115**, 153901 (2015).

[62] I. Söllner, S. Mahmoodian, S. L. Hansen, L. Midolo, A. Javadi, G. Kiršanskė, T. Pregnolato, H. El-Ella, E. H. Lee, J. D. Song,

S. Stobbe, and P. Lodahl, Deterministic photon-emitter coupling in chiral photonic circuits, Nat. Nanotechnol. **10**, 775 (2015).

[63] K. Y. Bliokh, F. J. Rodríguez-Fortuño, F. Nori, and A. V. Zayats, Spin-orbit interactions of light, Nat. Photon. **9**, 796 (2015).

[64] R. J. Coles, D. M. Price, J. E. Dixon, B. Royall, E. Clarke, P. Kok, M. S. Skolnick, A. M. Fox, and M. N. Makhonin, Chirality of nanophotonic waveguide with embedded quantum emitter for unidirectional spin transfer, Nat. Commun. **7**, 11183 (2016).

[65] P. Lodahl, S. Mahmoodian, S. Stobbe, A. Rauschenbeutel, P. Schneeweiss, J. Volz, H. Pichler, and P. Zoller, Chiral quantum optics, Nature (London) **541**, 473 (2017).

[66] M. Patterson, S. Hughes, S. Combrié, N.-V.-Q. Tran, A. De Rossi, R. Gabet, and Y. Jaouën, Disorder-induced coherent scattering in slow-light photonic crystal waveguides, Phys. Rev. Lett. **102**, 253903 (2009).

[67] P. D. García, S. Smolka, S. Stobbe, and P. Lodahl, Density of states controls Anderson localization in disordered photonic crystal waveguides, Phys. Rev. B **82**, 165103 (2010).

[68] B. Lang, D. M. Beggs, A. B. Young, J. G. Rarity, and R. Oulton, Stability of polarization singularities in disordered photonic crystal waveguides, Phys. Rev. A **92**, 063819 (2015).

[69] N. Mann, A. Javadi, P. D. García, P. Lodahl, and S. Hughes, Theory and experiments of disorder-induced resonance shifts and mode-edge broadening in deliberately disordered photonic crystal waveguides, Phys. Rev. A **92**, 023849 (2015).

[70] L. Zhou, H. Dong, Y.-X. Liu, C. P. Sun, and F. Nori, Quantum supercavity with atomic mirrors, Phys. Rev. A **78**, 063827 (2008).

[71] A. González-Tudela and J. I. Cirac, Markovian and non-Markovian dynamics of quantum emitters coupled to two-dimensional structured reservoirs, Phys. Rev. A **96**, 043811 (2017).

[72] A. González-Tudela and J. I. Cirac, Quantum emitters in two-dimensional structured reservoirs in the nonperturbative regime, Phys. Rev. Lett. **119**, 143602 (2017).

[73] M. Bello, G. Platero, J. I. Cirac, and A. González-Tudela, Unconventional quantum optics in topological waveguide QED, Sci. Adv. **5**, eaaw0297 (2019).

[74] E. Kim, X. Zhang, V. S. Ferreira, J. Banker, J. K. Iverson, A. Sipahigil, M. Bello, A. González-Tudela, M. Mirhosseini, and O. Painter, Quantum electrodynamics in a topological waveguide, Phys. Rev. X **11**, 011015 (2021).

[75] J. Koch, T. M. Yu, J. Gambetta, A. A. Houck, D. I. Schuster, J. Majer, A. Blais, M. H. Devoret, S. M. Girvin, and R. J. Schoelkopf, Charge-insensitive qubit design derived from the Cooper pair box, Phys. Rev. A **76**, 042319 (2007).

[76] Y. Chen *et al.*, Qubit architecture with high coherence and fast tunable coupling, Phys. Rev. Lett. **113**, 220502 (2014).

[77] F. Wulschner *et al.*, Tunable coupling of transmission-line microwave resonators mediated by an rf SQUID, EPJ Quantum Technol. **3**, 10 (2016).

[78] D. C. McKay, S. Filipp, A. Mezzacapo, E. Magesan, J. M. Chow, and J. M. Gambetta, Universal gate for fixed-frequency qubits via a tunable bus, Phys. Rev. Appl. **6**, 064007 (2016).

[79] B. Kannan, A. Almanakly, Y. Sung, A. D. Paolo, D. A. Rower, J. Braumüller, A. Melville, B. M. Niedzielski, A. Karamlou,

K. Serniak, A. Vepsäläinen, M. E. Schwartz, J. L. Yoder, R. Winik, J. I.-J. Wang, T. P. Orlando, S. Gustavsson, J. A. Grover, and W. D. Oliver, On-demand directional microwave photon emission using waveguide quantum electrodynamics, Nat. Phys. **19**, 394 (2023).

[80] D. F. James and J. Jerke, Effective Hamiltonian theory and its applications in quantum information, Can. J. Phys. **85**, 625 (2007).

[81] P. Roushan *et al.*, Chiral ground-state currents of interacting photons in a synthetic magnetic field, Nat. Phys. **13**, 146 (2017).

[82] T. Ramos, B. Vermersch, P. Hauke, H. Pichler, and P. Zoller, Non-Markovian dynamics in chiral quantum networks with spins and photons, Phys. Rev. A **93**, 062104 (2016).

[83] A. González-Tudela, C. S. Muñoz, and J. I. Cirac, Engineering and harnessing giant atoms in high-dimensional baths: A proposal for implementation with cold atoms, Phys. Rev. Lett. **122**, 203603 (2019).

[84] Y.-T. Chen, L. Du, L. Guo, Z. Wang, Y. Zhang, Y. Li, and J.-H. Wu, Nonreciprocal and chiral single-photon scattering for giant atoms, Commun. Phys. **5**, 215 (2022).

[85] C. Caloz, A. Alù, S. Tretyakov, D. Sounas, K. Achouri, and Z.-Lise Deck-Léger, Electromagnetic nonreciprocity, Phys. Rev. Appl. **10**, 047001 (2018).

[86] Y.-X. Zhang, C. R. i. Carceller, M. Kjaergaard, and A. S. Sørensen, Charge-noise insensitive chiral photonic interface for waveguide circuit QED, Phys. Rev. Lett. **127**, 233601 (2021).

[87] N. Gheeraert, S. Kono, and Y. Nakamura, Programmable directional emitter and receiver of itinerant microwave photons in a waveguide, Phys. Rev. A **102**, 053720 (2020).

[88] P. O. Guimond, B. Vermersch, M. L. Juan, A. Sharafiev, G. Kirchmair, and P. Zoller, A unidirectional on-chip photonic interface for superconducting circuits, npj Quantum Inf. **6**, 32 (2020).

[89] T. Shi, Y.-H. Wu, A. González-Tudela, and J. I. Cirac, Bound states in Boson impurity models, Phys. Rev. X **6**, 021027 (2016).

[90] S. Mahmoodian, M. Čepulkovskis, S. Das, P. Lodahl, K. Hammerer, and A. S. Sørensen, Strongly correlated photon transport in waveguide quantum electrodynamics with weakly coupled emitters, Phys. Rev. Lett. **121**, 143601 (2018).

[91] S. Mahmoodian, G. Calajó, D. E. Chang, K. Hammerer, and A. S. Sørensen, Dynamics of many-body photon bound states in chiral waveguide QED, Phys. Rev. X **10**, 031011 (2020).

[92] K. Kusmierek, S. Mahmoodian, M. Cordier, J. Hinney, A. Rauschenbeutel, M. Schemmer, P. Schneeweiss, J. Volz, and K. Hammerer, Higher-order mean-field theory of chiral waveguide QED, SciPost Phys. Core **6**, 041 (2023).

[93] J. R. Johansson, P. D. Nation, and F. Nori, QuTiP: An open-source Python framework for the dynamics of open quantum systems, Comput. Phys. Commun. **183**, 1760 (2012).

[94] J. R. Johansson, P. D. Nation, and F. Nori, QuTiP 2: A Python framework for the dynamics of open quantum systems, Comput. Phys. Commun. **184**, 1234 (2013).

[95] See, e.g., https://www.tek.com/en/products/signal-generators.